COBEM 2023 27TH INTERNATIONAL CONGRESS OF MECHANICAL ENGENEERING

ABCM Brazilian Society of Mechanical Sciences and Engineering
27th ABCM International Congress of Mechanical Engineering
December 04-08, 2023, Florianópolis-SC, Brazil

COB-2023-1519
CONVECTIVE PATTERNS IN HELE-SHAW FLOWS DRIVEN BY DENSITY GRADIENTS AND CHEMICAL COMPOSITION CHANGES

Bernardo Alberto Marcussi
André Celestino Martins
Rachel M. Lucena
Norberto Mangiavacchi
Rio de Janeiro State University, Rio de Janeiro, RJ, Brazil
marcussibernardo@gmail.com, amartins2295@gmail.com, rachel.lucena@eng.uerj.br, norberto@eng.uerj.br

Abstract. *The phenomenon of fluid displacement in porous media is of great practical interest for a variety of geophysical and environmental applications, such as Carbon Capture and Storage (CCS), oil recovery, water contamination, and granular flows, however studying this phenomenon in situ is extremely challenging. During displacement, convective flow patterns known as fingering have been observed and studied using the Hele-Shaw cell, an experimental device which replicates the porous media flow conditions found in nature, and may be used as a benchmarking tool for theoretical models and numerical simulations of fluid flow patterns against experimental data. The fluid flow behaviour in porous media can be explained by applying Darcy's law, provided that the solute hydrodynamic dispersion effect in the cell is taken into account. Therefore, this study involved the assembly of a Hele-Shaw cell to investigate the formation of flow patterns with fingering instability in density-driven flows in porous media generated by changes in chemical composition of the fluid medium. The cell consisted of two rectangular plates separated by seals and enclosing impermeable boundaries and an adjustable uniform gap with the upper boundary left open, where concentration gradients were generated and resulted in density gradients. Following an initial diffusive phase, the layer of heavy mixture thickened and developed instability, leading to the formation of finger-like structures and the flow evolution was recorded using a camera while the Hele-Shaw cell was illuminated from the backside with an array of LED lamps. The problem was characterised by three dimensionless parameters which determined the flow regime between the plates. The average finger tip flow velocity during the experiments was calculated and estimates derived from the Hele-Shaw equation were obtained. Furthermore, the concentration field and its derivative with respect to the width dimension of the cell were determined and yielded fluid vorticity. Thus, the stream function was determined by solving a Poisson equation and, finally, the velocity components in both the vertical and horizontal directions were computed and the derivative of concentration with respect to time was obtained. The average value of the integral concentration boundary layer thickness was also calculated. Thus, this study utilised a Hele-Shaw cell to replicate the two-dimensional fluid flow behaviour in porous media, providing valuable insights into the dynamic structures of gravity-driven porous media flows.*

Keywords: *Porous media, Hele-Shaw cell, fingering instability, velocity field*

1. INTRODUCTION

Geophysical phenomena associated with the displacement of liquids within porous media play a prominent role in both economic activities, such as oil recovery from reservoirs, and environmental endeavours, including the displacement of chemical contaminants in polluted areas, as well as the storage of greenhouse gas in saline aquifers and sea ice formation. In particular, investigations regarding the geological capture and sequestration of carbon dioxide have been increasingly garnering attention from both academia and industry.

Nevertheless, conducting *in situ* studies to examine the flow patterns that arise during these displacements presents significant challenges due to the extremely hostile nature of these environments. As a result, one potential alternative for investigating such phenomena is through experimental research. Experimental investigations aim to elucidate the flow phenomena associated with these activities by replicating the environmental conditions found in their respective locations, providing a highly intriguing approach. Furthermore, employing an experimental approach to studying the behaviour of these systems could yield novel insights and analyses pertaining to previously proposed theories.

The Hele-Shaw cell has been commonly used to study the displacement of fluids, in order to obtain qualitative and quantitative information about the flows present in various phenomena that occur in porous media, mimicking the flow conditions that occur in these transport phenomena. The Hele-Shaw apparatus consists of two flat, transparent, parallel plates that are fixed at a distance ranging from 0.1 mm up to 1.0 mm, forming a gap through which the fluids flow. It has been widely used as a low cost and highly effective experimental setup for the investigation of flow development

in porous media. Moreover, according to Alipour *et al.* (2020), the absence of laser sources and the presence of one low-speed camera make this method a safe and accurate alternative to classical PIV/PTV velocimetry processes.

There are many possible experimental setups for the Hele-Shaw cell and the displacement may occur by injecting the displacing fluid into a central orifice, as performed by Bunton *et al.* (2016), or through a side boundary, Chakraborty and Ramachandran (2021), but it also may occurr due to the emergence of concentration gradients, with a consequent change in the rheological parameters and properties of the fluids. When small perturbations of concentration and velocity fields occur at the interface, convective mixing is eventually produced (De Paoli *et al.*, 2022). The cell may be positioned in the vertical or horizontal directions, but may also be a diagonal cell. Mauger *et al.* (2016) carried out a study with a horizontal square Hele-Shaw cell fitted with four inlets and outlets, whereas Goyal *et al.* (2007) carried out a computational study based on the Stokes equations to investigate the effects of gravitational forces on miscible displacements in vertical Hele-Shaw cells. Experiments with the cell have been gaining modifications and improvements, adopting approaches that provide a better view of the phenomenon.

Some researches carried out with the cell have revealed convective patterns occurring during flows driven by density gradients that may be explained by the Darcy's law, provided that the solute hydrodynamic dispersion effect in the cell is taken into account, as described by Alipour *et al.* (2020). If density gradients are generated by changes in solute concentrations, instabilities will appear on the surface, after a brief period of diffusion, such as those that occur during the dissolution of carbonic anhydride in water or of salts in water. These instabilities will culminate in the development of descending advective currents, which became known as fingers, resembling finger-like projections. These perturbations grow and evolve into large finger-like convective structures (De Paoli *et al.*, 2022).

According to Saffman and Taylor (1958) a successful approach was adopted for providing derivation of the Darcy's law from the average of the Navier-Stokes equation with theoretical calculations. De Paoli *et al.* (2020) have confirmed experimentally that corrections can be applied to the Darcy's equation to recover the additional solute hydrodynamic dispersion and Letelier *et al.* (2019) have shown theoretically and numerically that corrections can be applied to the Darcy equation to recover the solute spreading induced by the hydrodynamic (Taylor) dispersion present in the Hele-Shaw flow regime.

In this work, a Hele-Shaw cell apparatus was assembled to study flow pattern formation with fingering instability in density driven flows caused by the effects of chemical composition changes in fluid medium. A Hele-Shaw flow regime was considered, the average flow velocity during the experiments was calculated, and estimates for the velocity field were made using the Hele-Shaw equation. Concentration field was inferred and the derivative of concentration with respect to the width dimension of the cell was obtained. Additionally, vorticity across the gap dimension was calculated, and the stream function was obtained by solving the Laplacian of the stream function. Finally, the velocity components in the vertical and horizontal directions were computed and the derivative of concentration with respect to time was obtained. The average value of the integral concentration boundary layer thickness was also calculated. Fingering instabilities were observed during the experiments with the cell and tracking of chemical composition changes enabled the reconstruction of the velocity field.

2. MATHEMATICAL MODELLING

The Hele-Shaw flow equation may be obtained from Navier-Stokes equation for incompressible newtonian fluid

$$\rho\frac{D\mathbf{v}}{Dt} = -\nabla p + \mu\nabla^2\mathbf{v} + \rho\mathbf{g}, \tag{1}$$

$$\nabla\cdot\mathbf{v} = 0 \tag{2}$$

where $\mathbf{v} = \mathbf{v}(x, y, z, t) = (v_x, v_y, v_z)$. Also, assuming a parabolic velocity profile

$$v_y(x, y, z, t) = \frac{4}{b^2} v_{y_{\max}}(x, y, t)\, z(b - z). \tag{3}$$

The second derivative of the y-velocity component with respect to z-direction is given by

$$\frac{\partial^2 v_y(x, y, z, t)}{\partial z^2} = -\frac{8}{b^2} v_{y_{\max}}(x, y, t), \tag{4}$$

and the average y-velocity (gap-averaged vertical velocity) is

$$\bar{v}_y(x, y, t) = \frac{1}{b}\int_0^b v_y(x, y, z, t)\, dz = \frac{2}{3} v_{y_{\max}}(x, y, t). \tag{5}$$

Upon replacing Eq. (5) in Eq. (4), we describe the second derivative of the y-velocity component as

$$\frac{\partial^2 v_y(x, y, z, t)}{\partial z^2} = -\frac{12}{b^2}\bar{v}_y(x, y, t). \tag{6}$$

Substituting Eq. (6) in the Navier-Stokes equation in y-direction Eq. (1), assuming that $D\mathbf{v}/Dt = 0$, that $v_z = 0$ and that the second derivatives of the y-velocity with respect to x and y are neglible, the Hele-Shaw equation may be obtained:

$$\bar{v}_y(x, y, t) = -\frac{b^2}{12\mu}\left(\frac{\partial p}{\partial y} - \rho g_y\right), \tag{7}$$

which gives the gap-averaged velocity in the y-direction. Analogously, the gap-averaged velocity in the x-direction is given by

$$\bar{v}_x(x, y, t) = -\frac{b^2}{12\mu}\frac{\partial p}{\partial x}. \tag{8}$$

Thus, the Hele-Shaw flow equation, in vector form, is

$$\bar{\mathbf{v}}(x, y, t) = -\frac{b^2}{12\mu}\left(\nabla p - \rho\mathbf{g}\right). \tag{9}$$

The Hele-Shaw equation determines the gap-averaged velocity field for a two-dimensional flow in a porous media and is identical with Darcy's law for motion in a porous medium of permeability, $b^2/12$, and may be used for the velocity field reconstruction of experiments carried out with the Hele-Shaw cell. This is an approximation valid when the gap or transverse dimension, b, is small compared with variations of scale in the lateral dimension parallel to the plates.

Assuming that the flow develops under the Hele-Shaw regime, and the density of the mixture is approximated as a linear function of solute concentration, Eq. (10), the calculation of the gap-averaged velocity field for the two-dimensional flow in the cell, considering the Boussinesq approximation, may proceed with equation(11)

$$\rho(C) = \rho(C_s)\left(1 + \frac{\Delta\rho}{C_s\rho(C_s)}(C - C_s)\right), \tag{10}$$

$$\bar{\mathbf{v}}(x, y, t) = -\frac{b^2}{12\mu}\left(\nabla P - \frac{\Delta\rho}{C_s}C\mathbf{g}\right). \tag{11}$$

The gradient of the difference between the current pressure of solution, p_c, and the hydrostatic pressure of pure water, p, is denoted by ∇P and represents additional buoyancy generated by salt dissolution. The density increase, $\Delta\rho$, is the difference between saturated solution and water; C is the concentration of salt dissolved in water; C_s corresponds to saturation concentration of potassium permanganate ($KMnO_4$) in aqueous solution; and $\frac{\Delta\rho}{C_s}C\mathbf{g}$ corresponds to weight increase per volume due to the salt dissolution.

Unbalanced weight and buoyancy forces originate downward fluid flow and rotating fluid motion along z- dimension. Taking the curl of equation (11) to obtain the vorticity of fluid about the gap dimension axis, ω_z, shows the direct proportionality between vorticity and the derivative of concentration with respect to the cell width dimension, which gives

$$\omega_z = \frac{b^2\, g_y\, \Delta\rho}{12\,\mu\, C_s}\,\frac{\partial C}{\partial x}. \tag{12}$$

Estimates for the concentration field and the derivative of concentration with respect to width dimension of the cell obtained from light transmitted may be made by post processing of a single image. Thus, vorticity across the gap dimension may be calculated and the stream function, ψ, obtained by solving the Poisson equation:

$$\frac{\partial^2\psi}{\partial x^2} + \frac{\partial^2\psi}{\partial y^2} = -\omega_z. \tag{13}$$

Finally, the velocity components in the vertical (y-direction) and horizontal (x-direction or cell width) directions may be calculated by the derivatives of the stream function defined as:

$$v_x(x, y, z, t) \equiv \frac{\partial\psi}{\partial y}, \qquad \text{and} \qquad v_y(x, y, z, t) \equiv -\frac{\partial\psi}{\partial x}. \tag{14}$$

2.1 Non-dimensional equations

The equations may be written in dimensionless form by choosing appropriate characteristic scales as $C_c = C_s$, the saturation value, $L_c = L_y$, the domain depth, $x^* = x/L_y$, $C^* = C/C_c$, and $V_c = b^2\Delta\rho g_y/12\mu$ to give

$$\omega_z^* = \frac{\partial C^*}{\partial x^*}. \tag{15}$$

Then, dimensionless stream function may be calculated by solving the Poisson equation

$$\frac{\partial^2\psi^*}{\partial x^{*2}} + \frac{\partial^2\psi^*}{\partial y^{*2}} = -\omega_z^* \tag{16}$$

and the derivatives of stream function lead to the reconstruction of dimensionless velocity field:

$$v_x^*(x,y,z,t) \equiv \frac{\partial \psi^*}{\partial y^*}, \qquad \text{and} \qquad v_y^*(x,y,z,t) \equiv -\frac{\partial \psi^*}{\partial x^*}. \tag{17}$$

Then, the dimensionless derivative of concentration with respect to time may be calculated from dimensionless velocity and concentration fields from a single snapshot

$$\frac{\partial C^*}{\partial t^*} = -\nabla^* \cdot \bar{\mathbf{v}}^* C^* + \frac{1}{ReSc} \nabla^{*2} C^*. \tag{18}$$

Moreover, the numerical calculation of the dimensionless derivative of concentration with respect to time may also be inferred by processing of consecutive images of the experiment, providing a different approach for the problem and a comparison between calculations via a single snapshot and via two different frames.

Additionally, as $t^* = t\,V_c/L_y$, the dimensionless derivative of the concentration with respect to time may be used to estimate the derivative of concentration with respect to time, as follows:

$$\frac{\partial C}{\partial t} = \left(\frac{C_s V_c}{L_y}\right) \frac{\partial C^*}{\partial t^*}. \tag{19}$$

Three dimensionless parameters may be used to verify the flow regime: the Rayleigh number, scaling relative strength of vertical advection and diffusion along the cell height

$$Ra = \frac{g \Delta \rho b^2 H}{12 \mu \gamma D}; \tag{20}$$

the ratio between the gap size and cell height

$$\epsilon = \frac{b}{\sqrt{12}\,H}; \tag{21}$$

and the combination of these two parameters, the anisotropy ratio A_r, which provides a parameter to determine the fluid flow behaviour, scaling the characteristic times of transverse diffusion and vertical advection:

$$A_r = \epsilon^2 Ra, \tag{22}$$

when $A_r = \epsilon^2 Ra \ll 1$, the flow regime is considered to develop under the Hele–Shaw regime. H denotes the cell height, b is the distance between the plates, μ is the viscosity, and D, the diffusion coefficient.

3. MATERIALS AND METHOD

In this research, a Hele-Shaw cell was assembled to study flow pattern formation with fingering instability in density driven flows triggered out by chemical composition changes initially introduced on the surface of fluid medium. The chemical composition change increased density on the surface, breaking vertical stability and disrupting buoyancy at the upper layer of water, making it sink and originating fingers. The Hele-Shaw apparatus assembled in this work consisted of two parallel plates that were fixed at a very small distance, forming a narrow gap through which fluid displacement was observed.

3.1 Experimental apparatus

The vertical configuration was chosen for the experimental setup and the cell consisted of two rectangular (27 cm $\times$ 20 cm) flat, transparent, 6 mm thick, polycarbonate plates separated by polyethylene terephthalate seals of 0.2 mm, and fixed by c-clamps on three sides, enclosing three impermeable side and bottom boundaries and a uniform gap. Since predictions made by the Darcy's law become more accurate for smaller gaps, the experimental setup was designed with an adjustable and narrow gap of approximately 0.4 mm. The domain dimensions are shown in Fig. 1 sketch.

The Hele-Shaw device was filled with water at room temperature, 20°C, and remained open at the top boundary where a steel mesh (200 μm grid size) was used to contain the compacted layer of potassium permanganate, assuring that the maximum solute concentration was kept constant, C_s at the top layer, during the experiments. Thus, density gradients were triggered out by composition changes at the upper layer of the aqueous phase, after the salt on the grid was soaked, and an initial diffusive phase occurred. Then, the layer of heavy mixture thickened, became unstable, and finger like structures were formed (Slim, 2014) and characterised the onset of convective downward flows.

Water was used as the lighter fluid and the heavier phase was formed as the potassium permanganate salt, $KMnO_4$, dissolved in the top layer of water and resembled finger-like structures. The three-dimensional space in the cell was described by the cartesian coordinate system: the x-axis corresponded to the cell width from left to right, the z-axis was transversal to the plates, and corresponded to the gap width direction, and the y-axis corresponded to the cell height dimension, the downward direction was taken as positive. As the cell was initially filled with water, the solute concentration C at time $t = 0$ was $C(x, y, z, 0) = 0$.

3.2 Image capturing and processing

The dissolution process of potassium permanganate at the upper layer of water in the cell was monitored employing a quantitative photographic technique and followed by post processing of the images, inferring concentration fields at high resolution from transmitted light intensity (Slim *et al.*, 2013; Ching *et al.*, 2017; De Paoli *et al.*, 2020). The time evolution of the flow was captured by a camera recorder (SAMSUNG 7.6 mm $\times$ 5.7 mm sensor, 2160p) at a rate of 30 f.p.s., with f/1.8 aperture, and 26 mm focal length to capture low-light situations, as the Hele-shaw cell was illuminated from the backside by an array of LED lamps. Experimental data for flow velocity field was generated and concentration changes were observed.

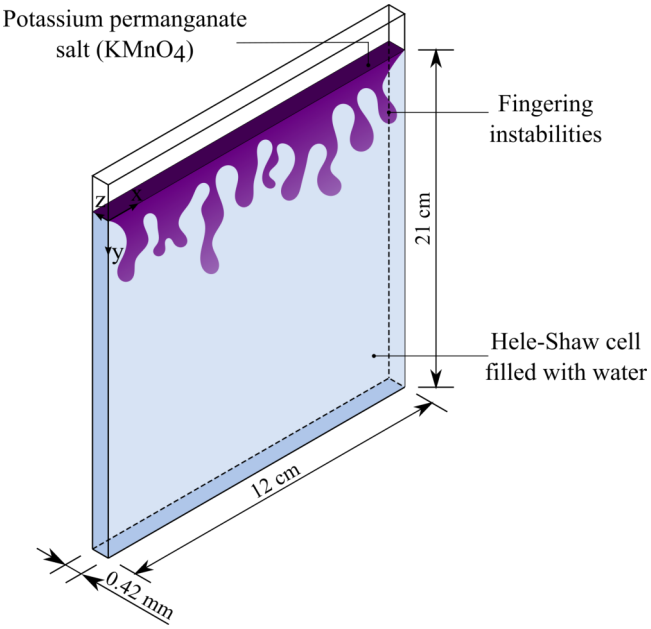

Figure 1. Sketch of the experimental apparatus with the Hele-Shaw cell dimensions.

The recovery of the stream function and the velocity field from the images were performed by several steps, beginning with the conversion of the original image to grey scale, as shown in Fig. 2. Since the RBG values of each pixel in a frame registered a concentration, the generated grey scale matrix was taken as the corresponded dimensionless concentration field, obtained for each frame, with the same resolution of the original image.

3.3 Numerical methods processing

The next step was to numerically calculate the source term of Eq. (15), ω_z^*, by estimates of dimensionless concentration field obtained for a single snapshot, using the Finite Element Method (FEM) and then solving Eq. (16) to yield the dimensionless stream function, ψ^*. The computation was performed by solving Eqs. (15)-(16), written in variational form, and discretised by the F.E.M. with Galerkin approximation.

Furthermore, velocity components were recovered from the the derivatives of stream function with respect to vertical and horizontal directions (y- and x-directions, respectively), Eq. (17), reconstructing the dimensionless velocity field. All data were obtained through image processing using Julia programming language.

The following step was the calculation of the dimensionless derivative of concentration with respect to time from reconstructed dimensionless velocity field and concentration data, from a single snapshot, neglecting fluid diffusivity and dispersion, by the advection-diffusion equation, Eq. (18). Moreover, finite difference method was also employed to provide a comparison between both numerical methods.

Additionally, image processing of two frames at different times, also provided an estimate for the derivative of concentration with respect to time using, for instance, the second order finite-difference approximation given by

$$\frac{\partial C^*}{\partial t^*} = \frac{C^*(t^* + \Delta t^*) - C^*(t^* - \Delta t^*)}{2\Delta t^*} + O(\Delta t^{*,2}). \tag{23}$$

Thus, a comparison between the two approaches, via a single snapshot and via two different frames, was carried out and provided an evaluation of the approach proposed in this work.

4. RESULTS AND DISCUSSION

4.1 Anisotropy ratio

The assembled Hele-Shaw tool was specially designed for mimicking Hele-Shaw flows in porous media and fluid flow in the cell was characterised by three dimensionless parameter for the values of the problem, as described in subsection 2.1. Estimates of water density were obtained for the experiments carried out under room temperature, 20°C, based on the correlations proposed by Novotny and Sohnel (1988). $KMnO_4$ has a bulk density of approximately 1602 kg/m^3 and its solubility in water, C_s, is 64 kg/m^3, at 20°C (WSA, 2016). The density of the saturated solution was calculated, and the density difference between the saturated solution and pure water obtained as $\rho_s - \rho_0 = 55$ kg/m^3. Viscosity and diffusion coefficient were assumed constant and independent of the solute concentration (Slim *et al.*, 2013), and medium porosity was taken as $\gamma = 1$. The experimental parameters adopted for the calculations are shown in Tab. 1.

Table 1. Physical properties.

Symbol	Property	Value
b	Gap width	0.42 mm
H	Domain height	21 cm
$\Delta\rho$	Density increase	55 kg/m^3
μ	Viscosity	1.002×10^{-3} Pa·s
D	Diffusivity	1.65×10^{-9} m^2/s
γ	Porosity	1.0

Hence, the calculations of the three dimensionless parameters described in subsection 2.1 yielded

$$Ra = \frac{g\Delta\rho b^2 H}{12\mu\gamma D} = 9.12841 \times 10^5, \quad \epsilon = \frac{b}{\sqrt{12}\,H} = 5.49857 \times 10^{-4} \quad \text{and} \quad A_r = \epsilon^2 Ra = 2.75991 \times 10^{-1}. \quad (24)$$

Therefore, the fluid flow in the cell was well characterised by a two-dimensional velocity field and the Hele-Shaw equation was applied for the calculations. Since $\epsilon^2 Ra \ll 1$, the Hele–Shaw flow regime took place and, thus only one finger have grown across the cell gap for $x-$ coordinate regions along the cell width.

Fluid flow behaviour in porous media tends to be described by Darcy's law of flow as the porous size tends to zero. In this situation, transverse diffusion across the cell is much greater than vertical displacement and a nearly flat wall-normal vertical velocity profile may be observed for fluid flow, with no considerable vertical dispersion by hydrodynamic motion. However, as this is an ideal situation, the real fluid flow behaviour in porous media is also associated with extra solute distribution that takes place during Taylor hydrodynamic dispersion, characterising the Hele-Shaw flow regime.

4.2 Concentration distribution

Movies at 30 f.p.s. were obtained with the apparatus and methodology described in the previous sections. The present analysis focused on a short segment of one movie, around 66 seconds after the start of the experiment, which was a representative example of the flow observed in the experiments. The colour image of one frame of the movie is shown in Fig. 2(a). The image shows a well contrasted image, with the finger-like structures of high concentration fluid moving downwards, against a clear background.

The development of coloured downward currents revealed the convective two-dimensional displacement patterns in porous media driven by concentration gradients, known as fingering instabilities, and is shown in Fig. 2(b) in grey scale image. The chemical composition change of fluid medium took place as the finger tips advanced from top to bottom and modified the entire domain colour as the experiment was carried out.

Various complex phenomena were clearly observed from the captured images, such as finger formation and evolution, tip splitting and finger merging. When tip splitting was observed, the growth of each split was unbalanced from the beginning, with some fingers assuming a negative velocity (upward motion) probably pushed up by extra pressure arisen as a reaction to the downward fingering instabilities, whereas others still moved down and enlarged. Shielding phenomena was also observed with larger finger preventing smaller ones to grow, and eventually making them fade away because of dilution provoked by upward currents of lighter fluid.

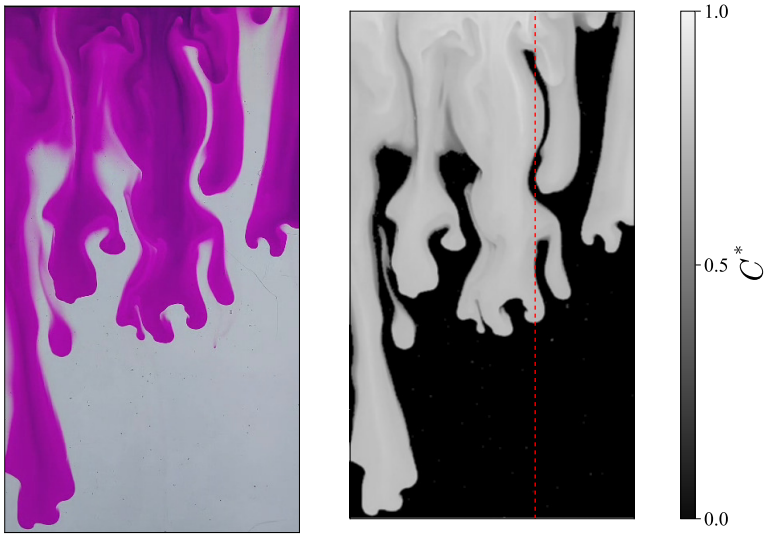

(a) (b)

Figure 2. Fingering instability captured by camera: (a) experimental image, and (b) grey scale. The vertical dotted red line in (b) shows the pixel column employed in the comparison of Fig. 4.

4.3 Average concentration

The average concentration in the horizontal direction, as a function of the vertical coordinate and time, can be computed by integrating the concentration distribution:

$$\bar{C}^*(y^*, t^*) = \frac{L_y}{L_x} \int_0^{L_x/L_y} C^*(x^*, y^*, t^*) dx^*. \tag{25}$$

The integral concentration thickness is defined by

$$\delta^*(x^*, t^*) = \int_0^1 C^*(x^*, y^*, t^*)\, dy^*, \tag{26}$$

and the average value of the integral concentration boundary layer thickness $\bar{\delta}_L(t)$ is, therefore

$$\bar{\delta}^*(t^*) = \frac{L_y}{L_x} \int_0^{L_x/L_y} \int_0^1 C^*(x^*, y^*, t^*)\, dy^* dx^*. \tag{27}$$

The evolution of the mass transport for the typical experiment under analysis can be visualised at various times, as shown in Fig. 3(a) for x-direction averaged concentration. It can be observed that, as the finger structures descend in the domain, the concentration boundary layer becomes thicker, until it reaches the bottom of the domain. The growth of the boundary layer $\bar{\delta}^*(t^*)$ can be observed in Fig. 3(b). The growth of the boundary layer starts to saturate at $t^* \sim 3$, when the fingers are reaching the bottom of the domain.

4.4 Finger tip descending velocity

Taking the concentration profile along the cross section shown in Fig. 2(b) at two different frames with a time interval of 2 seconds, as shown in Fig. 4 and considering a dimensionless concentration of 0.15, it was possible to measure the tip displacement. In this example, the tip displacement was $\Delta y = 2.10 \times 10^{-3}$ m, meaning the advance of this iso-concentration contour, and therefore resulting in an estimated tip velocity of $V_y = 1.05 \times 10^{-3}$ m/s. Considering a characteristic velocity $V_c = (4.2 \times 10^{-4})^2 \times 55 \times 9.81/(12 \times 10^{-3}) = 7.931 \times 10^{-3}$ m/s, the ratio between both could be calculated as 0.132.

4.5 Velocity field reconstruction

The dimensionless velocity field was reconstructed from estimated concentration profiles registered by grey scale, using the methodology described in Sections 2 and 3. The estimates for the dimensionless derivative of concentration with respect to the cell width, $\frac{\partial c^*}{\partial x^*}$, were obtained by analysing the light transmitted across the cell for a single snapshot and processing the images, as depicted in Figure 5(a). The dimensionless vorticity across the gap was then calculated using Eq. (15), and (b) the dimensionless stream function, ψ^*, was obtained by solving the Poisson equation Eq. (16).

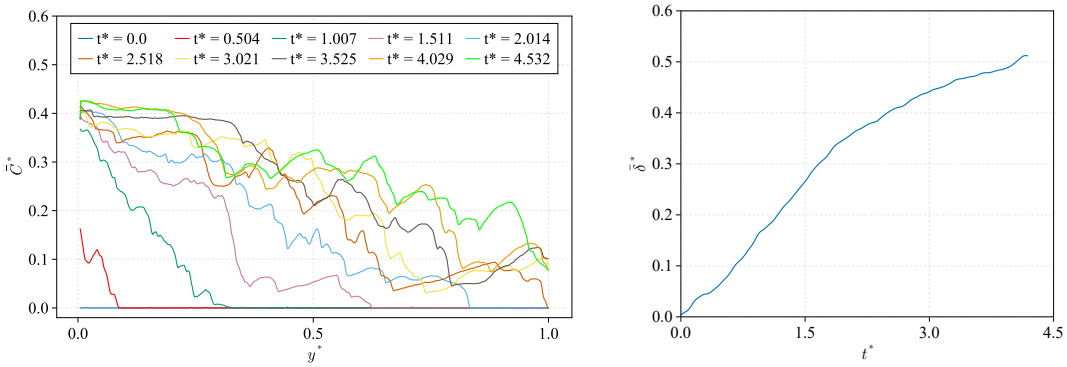

(a) (b)

Figure 3. Average concentration profiles: (a) average concentration profile $\bar{C}^*(y^*, t^*)$, and (b) boundary layer thickness $\bar{\delta}^*(t^*)$

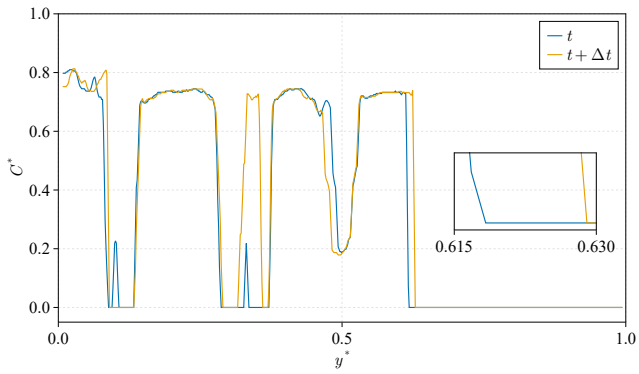

Figure 4. Comparison of concentration profiles at two times.

Finally, the dimensionless velocity components (c) in the horizontal (V_x^*) and (d) y-direction (V_y^*) were calculated as demonstrated, for a single frame.

The velocity plots revealed that between the descending regions (shown in red), which were associated with high concentration fingers, upward currents of clear liquid (depicted in blue) were observed. These upward currents developed in an analogous manner to the descending fingers and both motions were simultaneously coupled to produce the rotation of fluid across the cell gap axis.

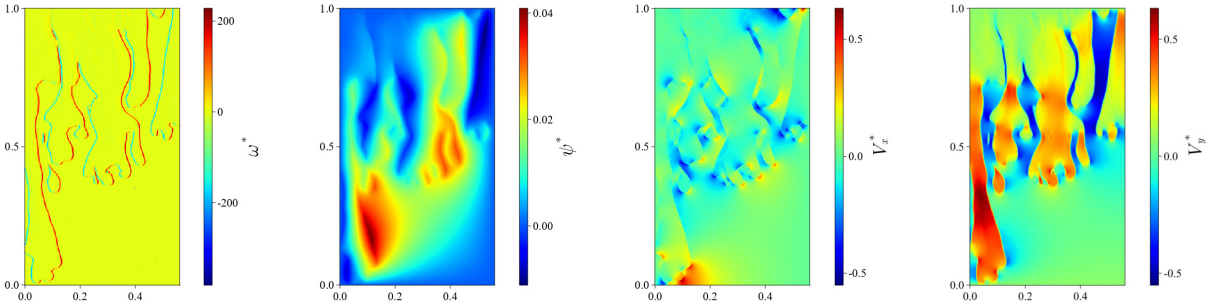

(a) $\omega^* \left(\text{or} - \dfrac{\partial c^*}{\partial x^*} \right)$ (b) ψ^* (c) V_x^* (d) V_y^*

Figure 5. Vorticity, stream function, and velocity dimensionless fields obtained after the reconstruction method employed for a single frame.

The velocity and concentration profiles at the red crossed line shown in Fig. 2(b), are shown in Fig. 6. It was observed that the velocity in the region of the tip, obtained from the reconstruction method, was $V_y^* = 0.33$, thus providing a quantitative validation of the methodology. On the other hand, it was observed that the regions between high density fingers had a large upward (negative) velocity. Similarly, in the region below the finger, for $y^* > 0.6$, the vertical component of the velocity was also negative. These regions of ascending flow are due to the conservation of mass of the

incompressible flow in the gap.

Additionally, the agreement between velocity and concentration profiles is most noticeable in Fig. 6, where the concentrations peaks were coupled with positive velocities (descending flow) and the lowest concentration values were associated to negative velocity values (ascending currents). Another remarkable feature seen in Fig. 6 is that higher velocities were observed for greater depths in the cell and top velocity was found for finger tip.

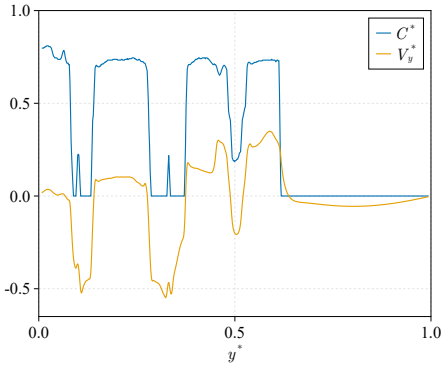

Figure 6. Dimensionless concentration C^*, and vertical velocity V_y^*.

4.6 Concentration time derivative

A comparison between both dimensionless derivatives of concentration with respect to time obtained by a single snapshot, Fig. 7 (a) and (b) (via velocity and concentration fields reconstruction, Eq. (18)) and by processing two different frames, Fig. 7 (c), Eq. (23) is provided below. Finger tip advance was observed for positive derivative, denoted in red in Fig. 7(a) and (b), and finger tip receding was observed for negative derivatives, denoted in blue. Both images exhibited remarkable similarity and demonstrated a strong agreement between the numerical approaches employed. However, Fig. 7(c) showed a difference in the dimensionless concentration compared to calculations made for a single snapshot and demands further investigation. Nevertheless, the observed agreement between the figures serves as a robust validation of the methodology utilised in this study.

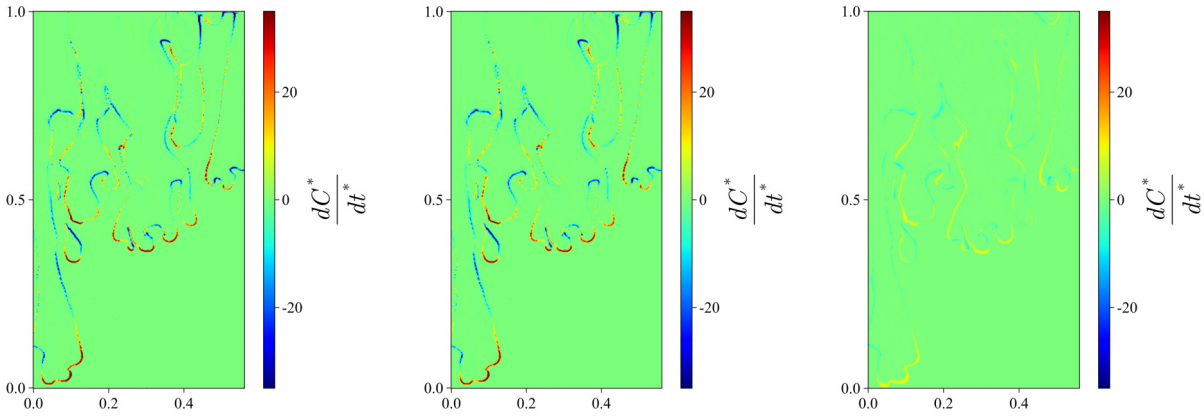

(a) (b) (c)

Figure 7. Comparison of the time derivative computed (a) from a single snapshot using F.E.M. and (b) using F.D.M., and (c) from two frames using second order finite-difference approximation.

5. CONCLUSION

A Hele-Shaw cell was assembled to study two-dimensional fluid flow dynamics in porous media, and the usage of a quantitative photographic technique followed by post-processing of the images permitted tracking of chemical composition changes. Furthermore, concentration field estimates obtained at high resolution from transmitted light intensity led to the reconstruction of the fluid velocity field.

The flow regime was described by the Hele-Shaw equation, and density-driven fingering instabilities were observed, revealing the convective patterns of fluid flow in porous media. The Hele-Shaw cell proved to be suitable for mimicking fluid flow behaviour in porous media, providing high-quality experimental data and featuring safety, low cost, and great

versatility.

6. ACKNOWLEDGEMENTS

The authors would like to acknowledge financial support from FAPERJ, CAPES, CNPq, and IFF (Fluminense Federal Institute).

7. REFERENCES

Alipour, M., De Paoli, M. and Soldati, A., 2020. "Concentration-based velocity reconstruction in convective Hele-Shaw flows". *Experiments in Fluids*, Vol. 61, pp. 1–16.

Bunton, P., Marin, D., Stewart, S., Meiburg, E. and De Wit, A., 2016. "Schlieren imaging of viscous fingering in a horizontal Hele-Shaw cell". *Experiments in fluids*, Vol. 57, pp. 1–11.

Chakraborty, S. and Ramachandran, A., 2021. "A macrotransport equation for the Hele-Shaw flow of a concentrated suspension". *Journal of Fluid Mechanics*, Vol. 924, p. A1.

Ching, J.H., Chen, P. and Tsai, P.A., 2017. "Convective mixing in homogeneous porous media flow". *Physical Review Fluids*, Vol. 2, No. 1, p. 014102.

De Paoli, M., Alipour, M. and Soldati, A., 2020. "How non-Darcy effects influence scaling laws in Hele-Shaw convection experiments". *Journal of Fluid Mechanics*, Vol. 892, p. A41.

De Paoli, M., Perissutti, D., Marchioli, C. and Soldati, A., 2022. "Experimental assessment of mixing layer scaling laws in Rayleigh-Taylor instability". *Physical review fluids*, Vol. 7, No. 9, p. 093503.

Goyal, N., Pichler, H. and Meiburg, E., 2007. "Variable-density miscible displacements in a vertical Hele-Shaw cell: linear stability". *Journal of Fluid Mechanics*, Vol. 584, pp. 357–372.

Letelier, J.A., Mujica, N. and Ortega, J.H., 2019. "Perturbative corrections for the scaling of heat transport in a Hele-Shaw geometry and its application to geological vertical fractures". *Journal of Fluid Mechanics*, Vol. 864, pp. 746–767. doi: 10.1017/jfm.2019.3. URL `https://doi.org/10.1017/jfm.2019.3`.

Mauger, C., Volk, R., Machicoane, N., Bourgoin, M., Cottin-Bizonne, C., Ybert, C. and Raynal, F., 2016. "Diffusiophoresis at the macroscale". *Physical Review Fluids*, Vol. 1, No. 3, p. 034001.

Novotny, P. and Sohnel, O., 1988. "Densities of binary aqueous solutions of 306 inorganic substances". *Journal of chemical and engineering data*, Vol. 33, No. 1, pp. 49–55.

Saffman, P.G. and Taylor, G.I., 1958. "The penetration of a fluid into a porous medium or Hele-Shaw cell containing a more viscous liquid". *Proceedings of the Royal Society of London. Series A. Mathematical and Physical Sciences*, Vol. 245, No. 1242, pp. 312–329.

Slim, A.C., 2014. "Solutal-convection regimes in a two-dimensional porous medium". *Journal of fluid mechanics*, Vol. 741, pp. 461–491.

Slim, A.C., Bandi, M.M., Miller, J.C. and Mahadevan, L., 2013. "Dissolution-driven convection in a Hele-Shaw cell". *Physics of Fluids*, Vol. 25, No. 2, p. 024101.

WSA, 2016. "Wsa 509 – potassium permanganate". Technical report, Water Security Agency, https://pdf4pro.com/cdn/wsa-509-potassium-permanganate-this-information-169789.pdf.

8. RESPONSIBILITY NOTICE

The authors are solely responsible for the printed material included in this paper.